Journal of Materials Research and Technology 30 (2024) 6596–6608

Contents lists available at ScienceDirect

Journal of Materials Research and Technology

journal homepage: www.elsevier.com/locate/jmrt

Hybrid manufacturing approach for landing gear applications: WAAM Ti–6Al–4V on forged Ti–5Al–5Mo–5V–3Cr

Calum Hicks [a,*], Saeed Tamimi [a,b], Giribaskar Sivaswamy [a,b], Misael Pimentel [a], Scott McKegney [a], Stephen Fitzpatrick [a]

[a] National Manufacturing Institute Scotland (NMIS), University of Strathclyde, Glasgow, United Kingdom
[b] Advanced Forming Research Centre (AFRC), University of Strathclyde, Glasgow, United Kingdom

ARTICLE INFO

Handling editorP Rios

Keywords:
Hybrid manufacturing
Wire-arc additive manufacturing
Direct energy deposition
Forging
Titanium alloys
Landing gear applications

ABSTRACT

High-strength metastable β-titanium alloys like Ti-5553 (Ti–5Al–5Mo–5V–3Cr) are frequently used in highly loaded aerospace components. Such aerospace parts tend to be expensive to traditionally manufacture due to current industry process limitations such as inflexibility for complex geometries, costs related to tooling for large forgings, extended lead times, poor machinability and high material waste. These challenges are leading to increased interest in exploring alternative manufacturing routes. This work investigates the use of additive manufacturing to deposit cost-effective and machinable Ti-64 (Ti–6Al–4V) alloy onto a forged Ti-5553 alloy substrate. The microstructure evolution, microhardness and tensile properties have been investigated for both the as-deposited as well as for stress relief heat-treated conditions. The results confirmed the formation of coarse columnar β grains with a fine basketweave α structure. The heat affected zones (HAZs) developed in the Ti-5553 substrate material from the cyclic thermal fluxes introduced from the melt-pool were characterized by a gradient microstructure of dissolving constituent phases with nearing proximity to the fusion zone. Tensile testing in the as-deposited condition was characterised with a UTS of 884 MPa and a ductility of 15%. Tensile samples extracted across the substrate-deposit interface all failed in the WAAM Ti-64 material and demonstrated comparatively greater strength but poorer ductility. A band of tensile residual stresses was imparted along the substrate, but was adequately stress relieved after heat-treatment at 600 °C. The heat-treatment led to the formation of more homogeneous α-phase laths throughout the HAZ of the Ti-5553 material and provided overall improvements to the strength and ductility.

1. Introduction

The Ti-5553 (Ti–5Al–5Mo–5V–3Cr) alloy is frequently used in high-strength aerospace applications such as the landing gear bogie beam because of its superior strength to density ratio and outstanding corrosion resistance. However, high production cost of the alloy [1], notorious machining difficulties [2], and poor buy-to-fly ratios [2] have sparked interest in alternative manufacturing routes for large forged aerospace components. Additive Manufacturing (AM) technologies are steadily gaining technology readiness levels and there is increasing interest from the aerospace industry in the possibility of a 'hybrid' manufacturing approach utilising Direct Energy Deposition (DED) technology to add features, such as a lugs, to forgings [3,4]. Here the term 'hybrid manufacturing approach' is used to indicate first using a forging to produce the bulk of the component, then adding features protruding from the forged geometry using DED [5]. In components produced with forged Titanium, the primary source of emissions come from raw material production [6]. Therefore, methods that enable near-net shape forgings to minimise material waste is an of interest to the manufacturing sector. As well as facilitating reduced forging complexity and machining requirements, a hybrid DED approach can be used to manufacture component features of dissimilar alloys to the base material [7], thus location specific mechanical properties can be tailored throughout the component. Such an example of interest is depositing the damage tolerant and cheaper Ti-64 (Ti–6Al–4V) alloy on to forged and heat-treated Ti-5553 substrate. Unlike Ti-64, Ti-5553 requires thermo-mechanical processing and heat-treatment below the β-transus temperature to achieve sufficient ductility to be used in real-world applications [8,9]. Such conditions are difficult to achieve with standard DED technology. Ti-64 on the other hand can achieve excellent ductility

* Corresponding author.
E-mail address: calum.hicks@strath.ac.uk (C. Hicks).

https://doi.org/10.1016/j.jmrt.2024.05.088
Received 29 February 2024; Received in revised form 2 May 2024; Accepted 11 May 2024
Available online 12 May 2024

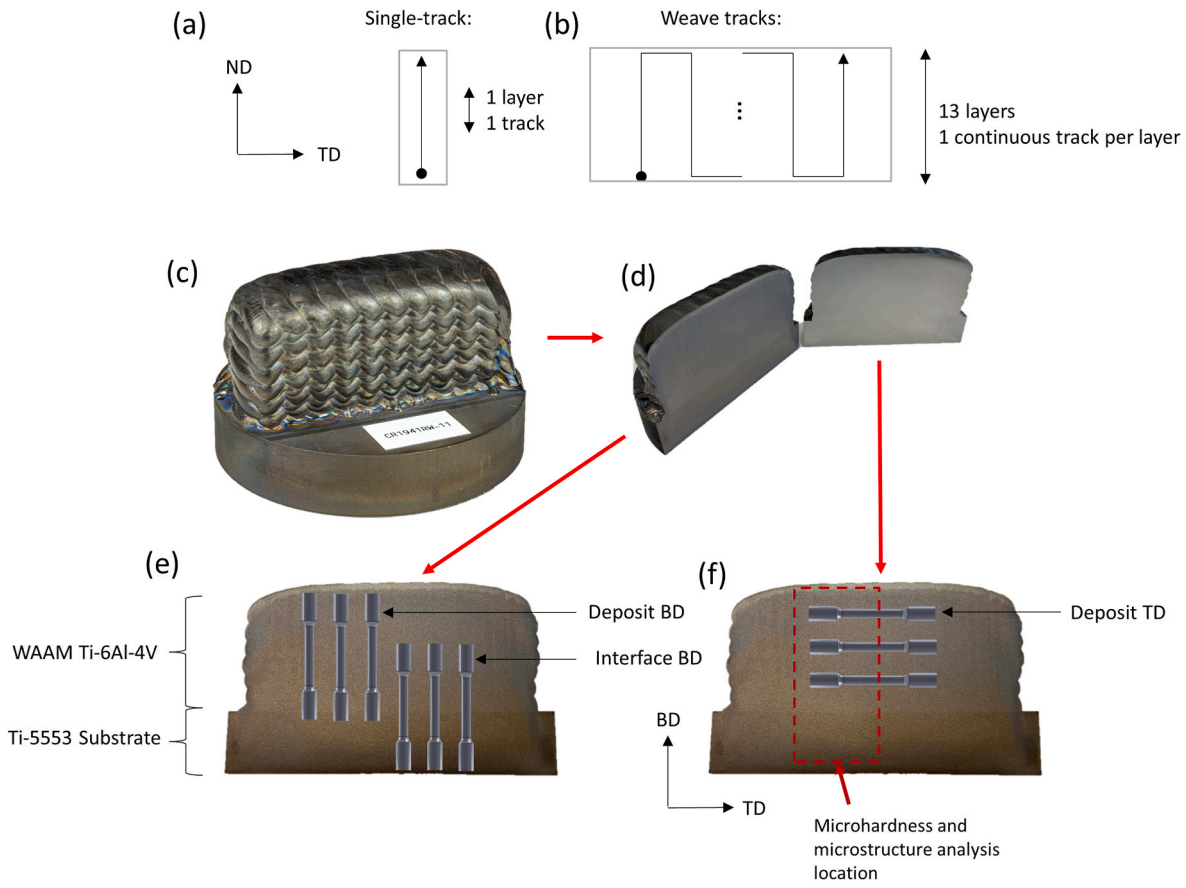

Fig. 1. Schematic illustrating dimensions of the deposition strategies and photographs showing the formed quality of manufactured AAC samples. Locations used for microstructure analysis, microhardness testing, as well as the orientations of the samples used for tensile tests are shown on photographs of the deposits.

Table 1
WAAM process parameters.

Process parameter	Value
Amperage	150 A
Travel Speed	5.9 mm s^{-1}
Wire Diameter	1.2 mm
Wire feed speed	66.7 mm s^{-1}
Layer height	3 mm
Track stepover	4 mm

and moderate strength when fabricated with DED making it more attractive to add features on Titanium forgings [10,11]. In the case of bogie beam manufacture, this could facilitate a reduced Ti-5553 forging size, reducing the cost of the expensive Ti-5553 material, as well as reducing the machining volume of the Ti-5553 material, in which tool life has been noted to be up to 100 times shorter than the Ti-64 alloy [12].

Wire and Arc Additive Manufacturing (WAAM), also known as DED-Arc, is one such DED technology that can be used to deposit high-density features on substrate material [13–15]. Compared to other DED technologies, such as Laser Metal Deposition (LMD), WAAM is particularly suited for the deposition of large-scale features with minimal gas induced porosities due to its high deposition rate [14,15]. Furthermore, the build envelope of WAAM is only limited by the span of a robotic arm and has been used to deposit features many metres in length [5,6]. Using a plasma arc to melt the feedstock, WAAM forms a melt-pool on a substrate material into which wire feedstock is fed. The plasma torch is connected to a robotic arm that facilitates translational motion based on 3D-CAD (computer aided design) data. Material is deposited in a layer-by-layer manner to obtain the near-net shape geometry followed by a subsequent final machining pass to obtain the required geometrical tolerances and surface finish [15]. Compared to similar AM technologies such as LMD, the melt-pool sizes involved in WAAM are typically much larger due to the high heat input of the plasma arc and are characterized with lower thermal gradients and slower cooling rates during solidification, typically of the order 10^2 K/s [13,16] compared to 10^3–10^4 K/s in LMD [13]. The large melt-pools induce substantial mixing effects, primarily due to the Marangoni force [13,17], causing a significant redistribution of alloying elements when joining dissimilar alloys [18,19]. Due to the high heat input and thermal cycling effect of multiple tracks and layers, WAAM components typically impart multiple large *heat affected zones* (HAZs) within the substrate and high peak tensile residual stresses [14,15,20].

Fabrication of WAAM Ti-64 components has seen attention from several researchers [10,11,16,20–26]. Columnar β grain growth often spanning many millimetres in length [10,11,16,20–26] with a strong ⟨001⟩ fibre texture parallel to the build direction (BD) [25] is ubiquitous. Formation of columnar β grains aligned with the build is attributed to the epitaxial growth phenomenon that occurs after remelting of the previous layer, far-field directional solidification conditions, and poor growth restriction factor of the alloy [27]. Evidence for formation of Basketweave α laths within the β grains and thin layer of α along the β grain boundaries (α_{GB}) throughout the deposit has already been reported [10,11,16,20–26]. Finer α morphology, or even martensitic α′, have been reported within the initial layers due to faster cooling rates experience during the deposition process [10,24].

A key characteristic of meta-stable β alloys such as Ti-5553 is the suppression of the β → α transformation upon quenching from temperatures above the β-transus [28] (856 °C for Ti-5553 [29]). The slow α transformation kinetics in the Ti-5553 alloy is attributed to the

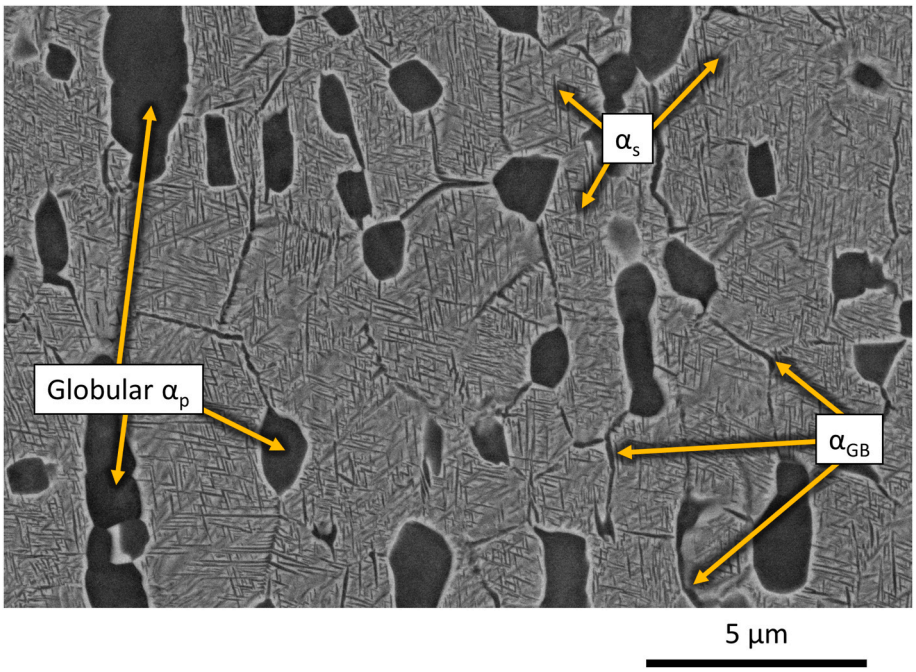

Fig. 2. Micrograph of the as-forged and STA heat treated Ti-5553 substrate showing the presence of globular α_p and equiaxed β sub-grains filled with fine α_s laths. A fine film of α_{GB} can be seen lining the β sub-grain boundaries.

concentration of slow diffusing solutes such as molybdenum [30]. Monolithic Ti-5553, consisting of β-grains devoid of any α-phases, is characterized with moderate tensile strength of ≈768 MPa and good ductility of 13%–22% [31–34]. The size of β grains has notable influence on the tensile elongation, with finer grain sizes exhibiting greater ductility [9,35]. By ageing within the α+β phase regime, α phase can be precipitated homogenously throughout the β matrix to high volume fraction as fine acicular laths. Precipitation of the α laths can either form on metastable nano-scaled ω precipitates that form upon quenching from above the β-transus temperature [36] or directly from compositional fluctuations within the grains of β-phase, known as the spinodal decomposition mechanism [37]. Nano-scaled ω precipitates are generally undesirable due to their embrittling effect [9]. The size and volume fraction of α laths can be modified by controlling the ageing time and temperature [38,39]. A continuous film of α_{GB} can form along prior-β grain boundaries and is coarsened through a diffusion-controlled process as solutes of β-stabilising elements such as Molybdenum are rejected into the adjacent β matrix [40]. This β-stabiliser enriched region is termed a *precipitate free zone* (PFZ) and is notorious for easy crack growth and brittle fracture behaviour due to its moderately relative softness compared to the adjacent α_{GB} [31,41–43]. Thermo-mechanical treatment such as forging can introduce globular primary α (α_p) precipitates and fine β sub-grains. After forging, a solution and ageing treatment within the α+β phase region provides a desirable microstructure of fine equiaxed β grains filled with globular α_p and fine acicular secondary α (α_s) laths with in fine the β sub-grains, often termed a *bi-modal* microstructure. Such a microstructure is attributed with an excellent combination of strength and ductility [8,9] and serves as the basis for bogie beam design. The globular α_p precipitates accommodate plastic deformation [8,9,44] and break up the continuous film of α_{GB} that can be deleterious to the ductility [9,28].

In an investigation of an *alloy-alloy composite* (AAC) of WAAM Ti-64 layers deposited on to WAAM Ti-5553, a stepwise microstructure transition spanning several layers from the Ti-5553/Ti-64 interface was noted [18]. This was determined to be predominantly driven by the unique discrete chemical compositions located within each deposited layer arising from the re-melting and melt-pool mixing effects between the depositing layer and previous layer. During deposition of the initial Ti-64 layer on the Ti-5553 substrate, significant mixing of β stabilising elements reduced the size of the α laths precipitated in the β matrix. This effect is diluted with each subsequent deposited layer of Ti-64 [18].

The above research indicates that an AAC of WAAM Ti-64 and WAAM Ti-5553 can provide good metallurgical bonding. However, the microstructure of forged Ti-5553 with a bi-modal microstructure significantly differs from the lamellar microstructure of WAAM Ti-5553. Therefore, this paper aims to investigate the effect of WAAM Ti-64 deposition onto forged and heat-treated Ti-5553 substrates, including after a tailored post-deposition stress relief heat-treatment. Room temperature tensile behaviour have been investigated for both the Ti-64 deposit, as well as across the interface between the Ti-64 and Ti-5553 by testing samples extracted from multiple orientations with respect to build direction.

2. Material and methods

2.1. Wire-Arc Additive Manufacturing process

The substrate material used in this study was extracted from a solution-treated and aged Ti-5553 bogie beam forging. For greater clarity on the microstructure evolution that occurs during the deposition of multiple tracks and layers, an additional sample was prepared involving a single-track deposit of Ti-64. Samples of Ti-64 were deposited on separate substrate sections using the deposition strategy outlined in Fig. 1, and using the WAAM process parameters outlined in Table 1. The substrates were of 100 mm diameter and 19 mm thickness. Commonly referred to as a 'weave' strategy, the deposition path follows a zig-zag pattern across the wall length as shown schematically in Fig. 1. Therefore, each layer is deposited as one continuous track. Each deposited layer was of 90 mm and 30 mm. 13 layers were deposited with a 3 mm step height, producing a build of ≈40 mm height.

2.2. Heat treatment and metallurgical investigation

After deposition, some samples were taken for stress-relief heat treatment. These samples were coated with Deltaglaze, a glass based protective coating, for atmospheric protection and then aged in a

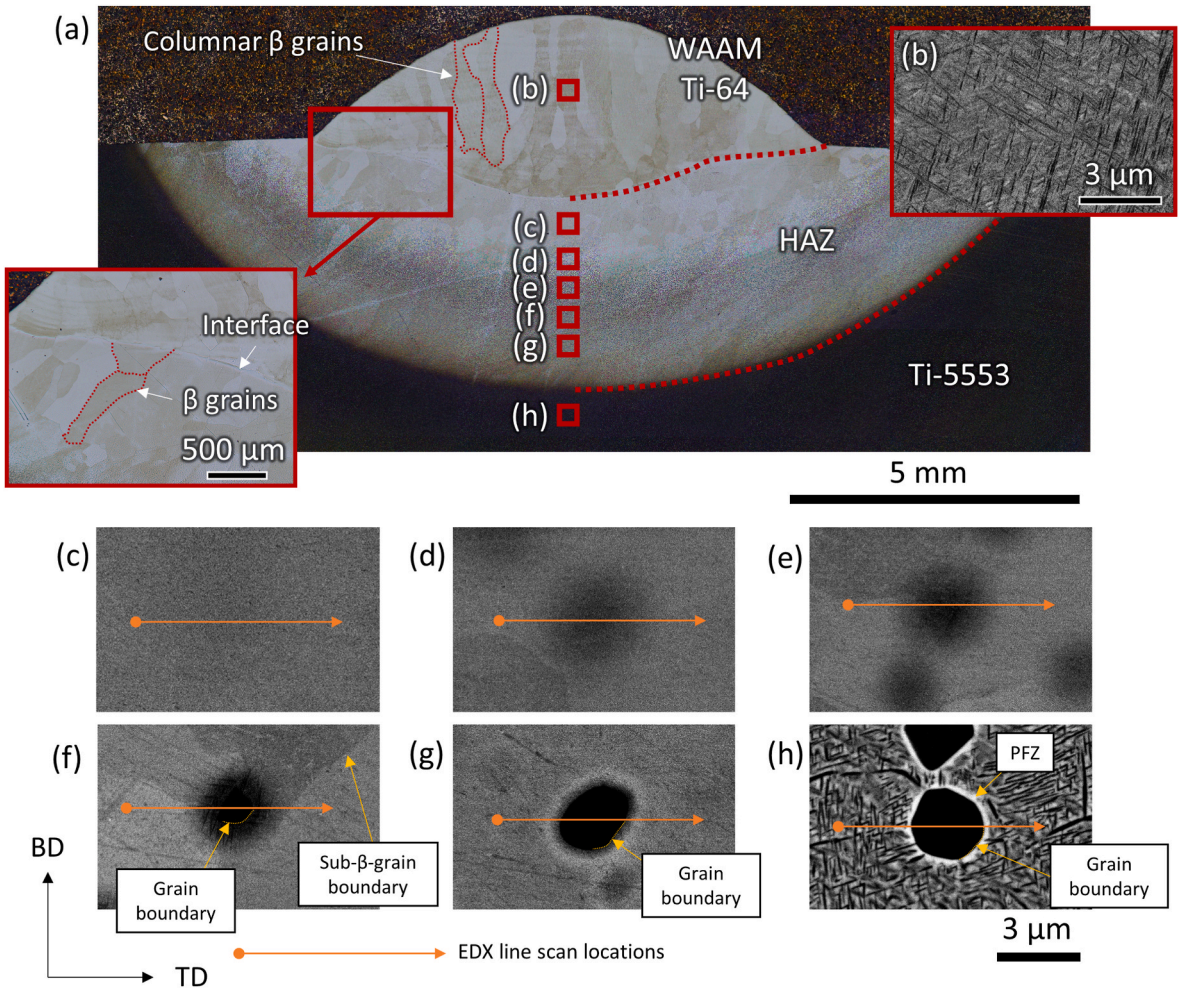

Fig. 3. (a): Montage of optical macrographs showing macrostructure of the single-track Ti-64 deposit and Ti-5553 substrate. (b–h): High magnification back-scatter SEM micrographs of the regions annotated in (a) showing the microstructure of the Ti-64 deposit and the dissolution aspects of the globular α_p grains.

Carbolite furnace. The stress-relief treatment parameters were decided after investigation of the as-deposited samples and consisted of soaking the sample at 600 °C for 8 h followed by air cooling back to room temperature. The heat-treatment temperature was selected to provide sufficient temperature to stress relieve the part, precipitate α phase homogeneously in the HAZ of the Ti-5553, whilst also avoiding dissolution of the globular α phase and fine sub-β-grains of the forged Ti-5553 substrate.

For analysis of the cross-sectional residual stresses, the contour method was applied. For a full description of the contour method, the reader is referred to Refs. [45,46], however, the salient points will be described here. Blocks were sectioned using wire electro-discharge machining (w-EDM), using a 250 μm brass wire in a low power 'skim' mode along the TD axis to produce the cross-sectioned faces as shown in Fig. 1. Both faces were measured using a Mitutoyo Crysta Apex C coordinate measuring machine (CMM) with a ruby touch probe. A grid of points was mapped and measured over the cross-sectioned surface with a 300 μm spacing in both directions. After measurement, a representative 3D finite element model of the cross-sectioned parts was created in ANSYS Workbench software. The geometry was meshed using hexahedral elements mapped across the cross-sectioned part surface and swept through the thickness. Once meshed, the node positions and CMM measurements were imported into MATLAB. First the CMM data sets from each face are aligned to a common coordinate system. Secondly, the data sets are conservatively cleaned to remove any data outliers or surface artefacts introduced from the w-EDM cut. The data sets are then combined and averaged, and a mathematical surface of bivariate cubic splines are fitted to the data in a piecewise manner. A knot spacing of 3.33 mm in both directions was used as a compromise between under or overfitting of the CMM data. Finally, the out-of-plane displacement at the FE node locations were evaluated on the fitted surface, reversed, and then exported back to the FE model as nodal displacements. Once appropriately constrained, the FE model was used to calculate the residual stresses across the cross-sectioned face using a young's modulus of 110 GPa.

Samples for microstructure and microhardness investigations were extracted from the annotated region shown in Fig. 1. Round bar tensile coupons with a gauge length and diameter of 16 mm and 4 mm respectively were extracted from the deposited WAAM Ti-64 in both BD and TD orientations as schematically shown in Fig. 1. Additionally, tensile coupons were also extracted aligned in the build direction with their gauge length spanning across the interface between the WAAM Ti-64 and Ti-5553 substrate. Three samples were tested for each condition. Tensile tests were conducted at room temperature at a strain rate of 1 mm/min using screw driven Zwick/Roell Z250 machine and samples were taken up to fracture.

All specimens for microstructure and microhardness analysis were prepared using standard metallographic preparation techniques of mounting and mechanical polishing, followed by vibratory polishing in 0.25 μm colloidal silica suspension. For optical microscopy analysis, samples were etched using Kroll's reagent and micrographs recorded using a Leica DM12000 M microscope. Macrographs were compiled

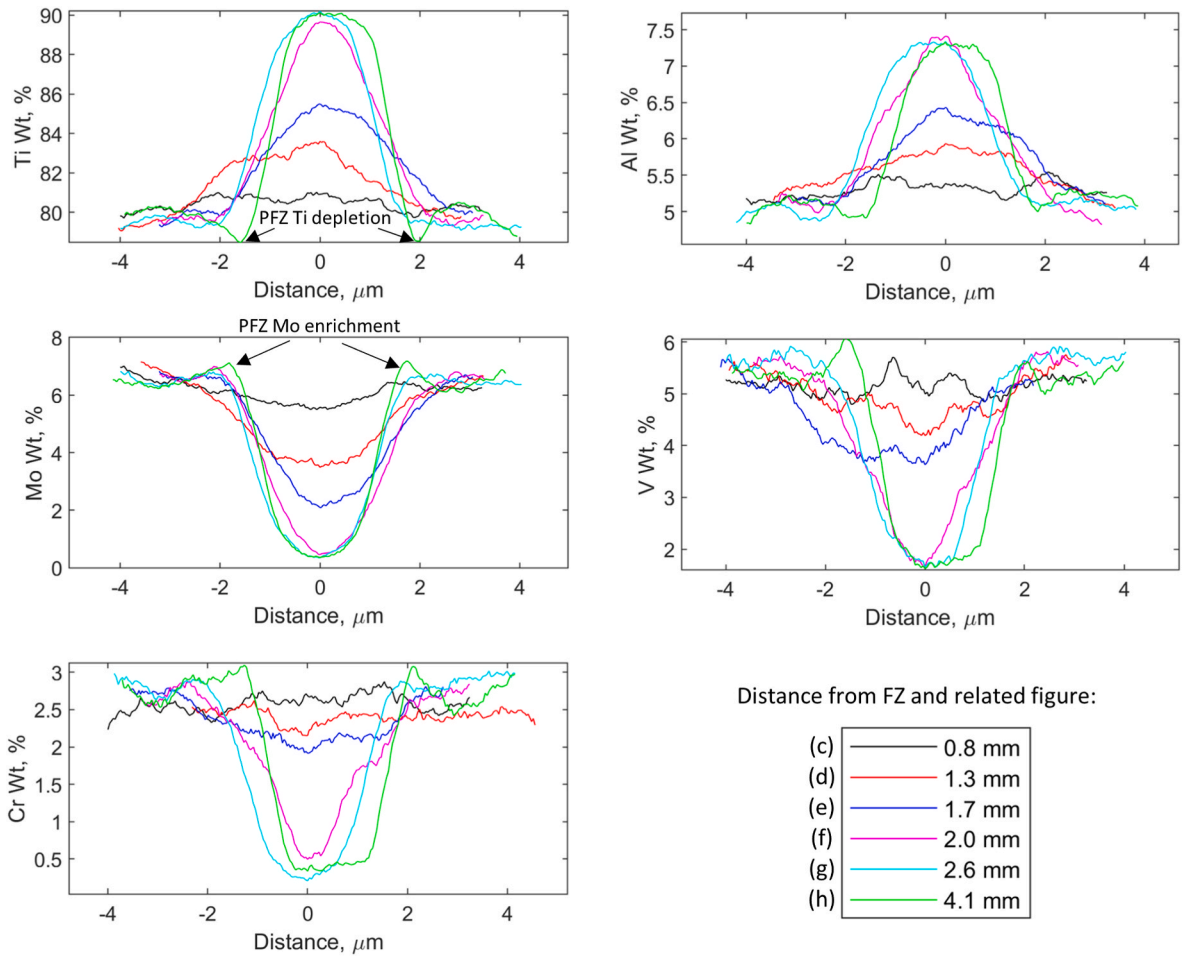

Fig. 4. Elemental distribution of alloying elements recorded by EDX line scan analysis along the direction indicated by the orange arrows in Fig. 3(c–h).

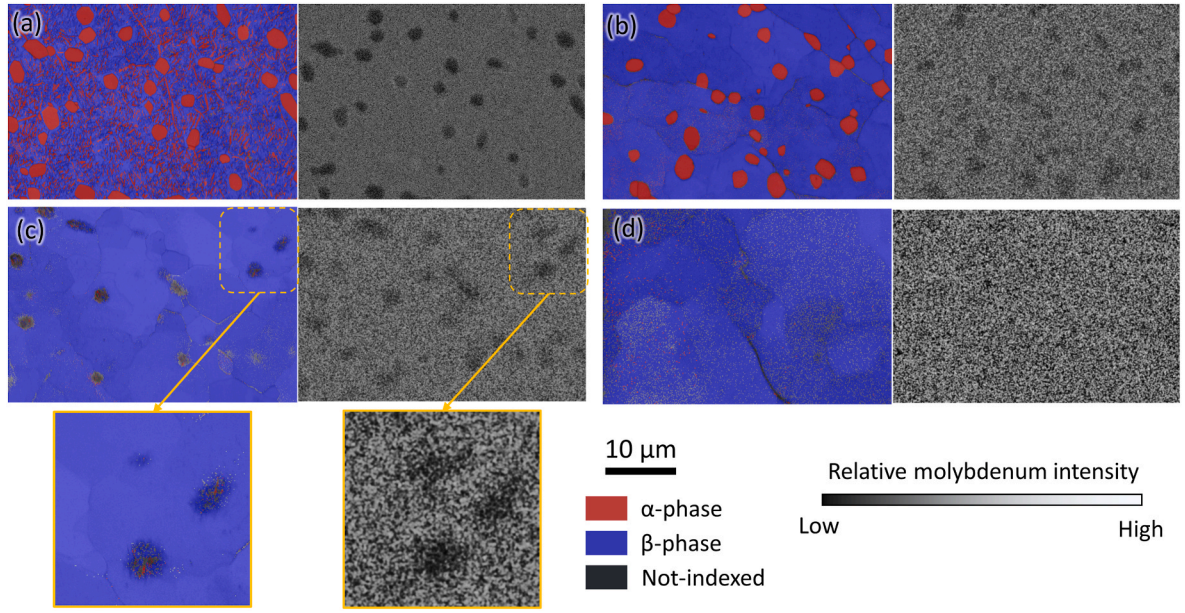

Fig. 5. Combined EBSD and EDX investigation of single-track specimen HAZ. (a) 4.1 mm from FZ, (b) 3.0 mm from FZ, (c) 1.7 mm from FZ, and (d) 0.8 mm from FZ.

automatically from a spatial grid of low magnification micrographs using Leica LAS software.

Vickers microhardness measurements were carried out using a DuraScan 70 G5 hardness tester at a load of 1 kg (HV1) for 10 s across a mapped grid of indents with a spacing of 3 mm in both the BD and TD directions. Microhardness contour plots were generated using MATLAB.

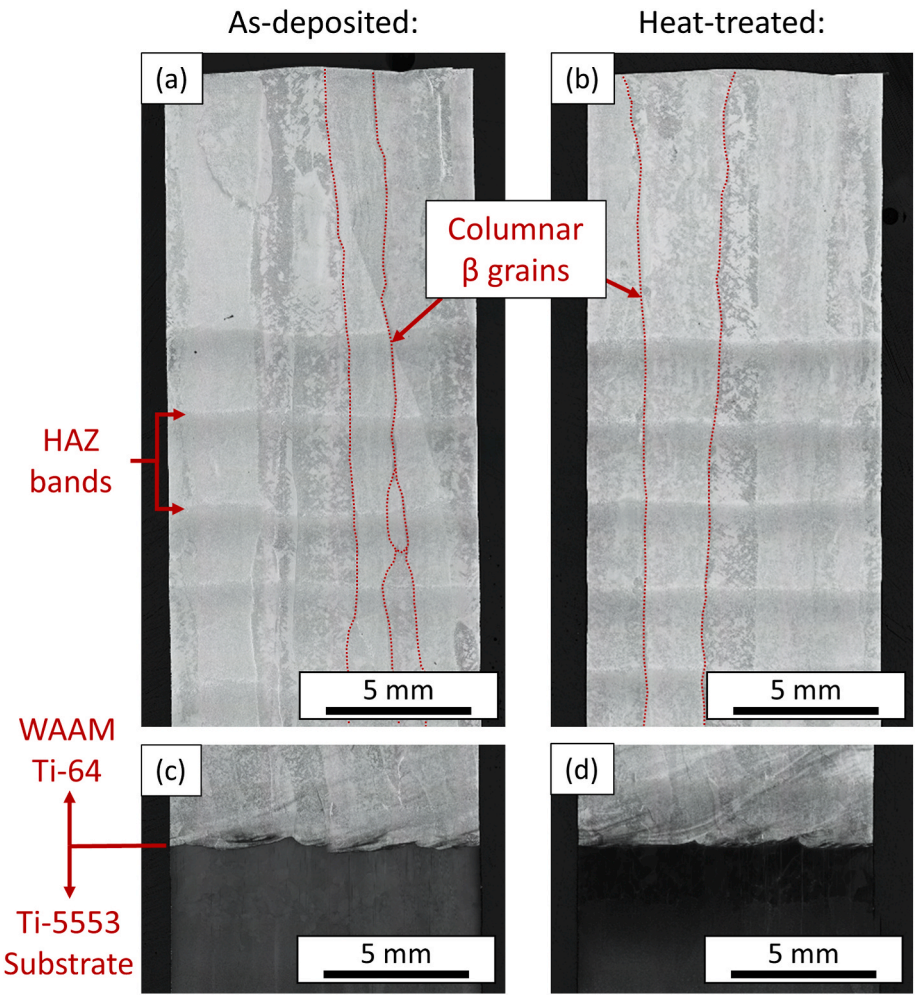

Fig. 6. Optical macrography of as-deposited and heat-treated samples. The top of the deposits are presented in (a–b), and the substrate interface for both samples are presented in (c–d).

SEM micrographs have been recorded using a FEI Quanta 650 microscope at a 15-kV working voltage and 4.0 μm spot-size. Electron backscatter diffraction (EBSD) analysis has been recorded using an Oxford Instruments detector with a step size of 50 nm. Post processing of the EBSD data was completed in HKL Channel5 software. The distribution of key alloying elements was analysed using an Oxford Instruments X-Max 50 mm^2 energy dispersive X-ray (EDX) spectrometer. For plotting the alloying element distributions from the linear EDX scans, noise has been conservatively removed from the raw EDX data. The noise reduction algorithm uses a moving window to calculate the value for each point based on the median of the surrounding data points within the sample window.

3. Results and discussion

3.1. Initial Ti-5553 substrate microstructure

The substrate material used for this study was extracted from a solution-treated and aged (STA) Ti-5553 bogie beam forging. The microstructure of the as-received Ti-5553 is presented in Fig. 2 and consists of fine β-sub-grains lined with a thin film of α_{GB} and coarse globular α_p grains. A homogeneous dispersion of fine acicular α_s laths fill the β sub-grain interiors. The total α phase fraction was 52.6% ± 0.7%. The globular α_p grains account for 12.3% fraction and are of an average 1.98 μm size, whilst the α_{GB} was measured to be 0.13 μm average thickness. The average microhardness of the substrate was measured to be 408 ± 5 HV.

3.2. Microstructure characteristics of the single-track Ti-64 deposit

Microstructural aspects of the single-track of Ti-64 deposited on the Ti-5553 substrate is presented in Fig. 3a. Three distinct regions can be observed: the WAAM Ti-64 track, the HAZ in the Ti-5553 substrate, and the base metal (BM) of the Ti-5553 substrate. Compared to the Ti-64 track and Ti-5553 HAZ, the Ti-5553 BM has reacted much more strongly with the chemical etchant, producing the dark contrast of this area. Coarse columnar β grains are observed within the Ti-64 track, with some of these annotated with the red dotted lines in Fig. 3a. High magnification SEM micrographs recorded from five locations along the build direction are presented in Fig. 3b–h, and are based on the approximate locations (Fig. 3a). The microstructure of the WAAM Ti-64 single-track (Fig. 3b) revealed a fine α and martensitic α′ morphology within the columnar β grains of the deposit. The formation of these fine α morphologies is likely due to the fast-cooling rate within the melt-pool following solidification.

The HAZ was characterized with a gradient microstructure from the α-phase rich Ti-5553 BM (Fig. 3h), to the apparent monolithic β-phase microstructure adjacent to the fusion zone (FZ) (Fig. 3c). Apparent growth of β grains adjacent to the FZ can be observed in the inset optical micrograph of Fig. 3a indicating exposure to temperatures exceeding the β-transus temperature. The gradient microstructure can be attributed to the variation in thermal history due to the heat flux from the deposition

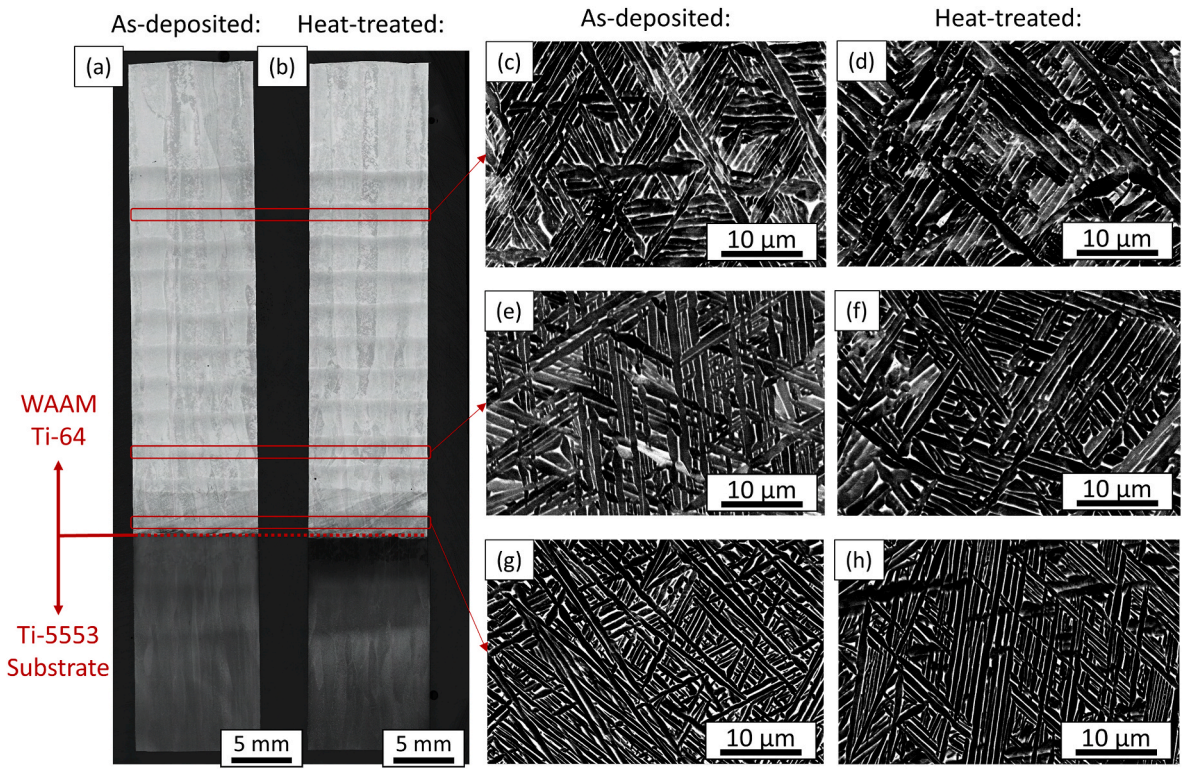

Fig. 7. (a–b): Macrographs showing approximate locations of representative SEM micrographs captured at locations through the build direction of the WAAM Ti-64 in (c–h) for both as-deposited and heat-treated samples.

of the Ti-64 track. HAZ locations near the FZ have experienced much larger peak temperatures compared to locations at the extent of the HAZ/base metal boundary. Fig. 3g and h demonstrate that the fine scale α_s laths dissolve at lower temperatures compared to the globular α_p grains. This is concurrent with observations by Chen et al. [47] who reported that the temperature for initial dissolution is 515 °C for α_s laths, and 702 °C for globular α_p grains. This behaviour was attributed to the difference in chemical compositions between the α_s and α_p phases and the high curvature of the acicular α_s lath tips [47]. The thermodynamic stability of interfaces with high curvature is reduced due to the Gibbs-Thomson effect [47,48].

The micrographs presented in Fig. 3c-g show α_p grains undergoing progressive stages of dissolution. In order to further understand the dissolution of the globular α_p grains, EDX line scans have been recorded over the regions marked in Fig. 3c-h and are presented in Fig. 4. The α_p grains of the base metal (Fig. 3h) appear with a well-defined boundary under back-scatter SEM imaging and are surrounded by a PFZ enriched with β-stabilising elements rejected from the α_p grain to give the prominent white contrast in the back-scatter SEM micrograph. The minor Mo enrichment and Ti depletion within the PFZ can be observed in the EDX line scan data presented in Fig. 4. In Fig. 3g, the α_p grain appears to have receded in size leaving a diffuse boundary between the α_p and β matrix. It is evident from the micrograph presented in Fig. 3f that the grain of the α_p appears to have moderately receded in size, leaving behind an area of dark contrast still visible with back-scatter SEM indicating incomplete homogenisation of the diffusing solutes from the dissolving α_p grain into the surrounding β matrix. This is also confirmed from the recorded EDX elemental distributions of Fig. 4. In the micrographs presented in Fig. 3d and e, the α_p appears to have completely dissolved, but leaving a diffuse area still visible with back-scatter imaging. The recorded EDX elemental distributions for these areas reveal prominent chemical segregation is still present. Within a proximity of 0.8 mm to the FZ (Fig. 3c), the diffuse solute enriched areas are no longer visible with back-scatter SEM, indicating local homogenisation of the solute elements and confirmed with the elemental distribution recorded using EDX. These findings are concurrent with the dissolution of α_p phases as a diffusion-controlled transformation. With increasing proximity to the FZ, the material experiences higher peak temperature from the heat flux conducted from the melt-pool. The mobility of the diffusing solutes is enhanced at higher temperatures [49], but because of the high heating and cooling rate, the exposure time at peak temperatures is very short. In Fig. 3d-e, despite the apparent phase transformation of α→β, the long-range diffusion of solutes is limited in the surrounding β matrix, leading to the observed local diffuse concentration of alloying elements. This is often referred to as 'ghost-α' and is frequently observed in the HAZ of weldments [4, 50–52]. Furthermore, in-situ measurements captured during continuous heating and cooling cycles of the Ti-5553 alloy using high-temperature laser-scanning confocal microscopy revealed that the ghost-α phenomenon can still be visible at temperatures up to 1400 °C [53].

To further investigate the observed 'ghost-α' phenomenon, combined EBSD and EDX maps of areas throughout the HAZ are presented in Fig. 5. At 4.1 mm from the FZ, both globular α_p and fine acicular α_s phases have been indexed (Fig. 5a) and the corresponding EDX element distribution map confirms a depletion of molybdenum within the globular α_p grains. At 3 mm from the FZ, α_s has dissolved but the globular α_p are still present (Fig. 5b). The stage of α_p grain dissolution can be observed in Fig. 5c as proximity to the FZ is closer. At this proximity to the FZ, almost no α phase has been indexed, yet some diffuse unindexed regions are present and remain depleted in molybdenum (Fig. 5c). Furthermore, as visible in the magnified region of Fig. 5c, the diffuse prior-α_p regions are frequently indexed as β phase, yet still display a depletion of molybdenum which is consistent with ghost-α characterisation. Finally, at 0.8 mm distance from the FZ, diffuse unindexed regions are no longer visible and a homogeneous dispersion on molybdenum is indicated by the EDX map (Fig. 5d). It is unclear as to why EBSD is frequently unable to index the diffuse regions surrounding dissolving α_p grains. This may be due to a change in lattice parameters due to solute enrichment, or possibly the

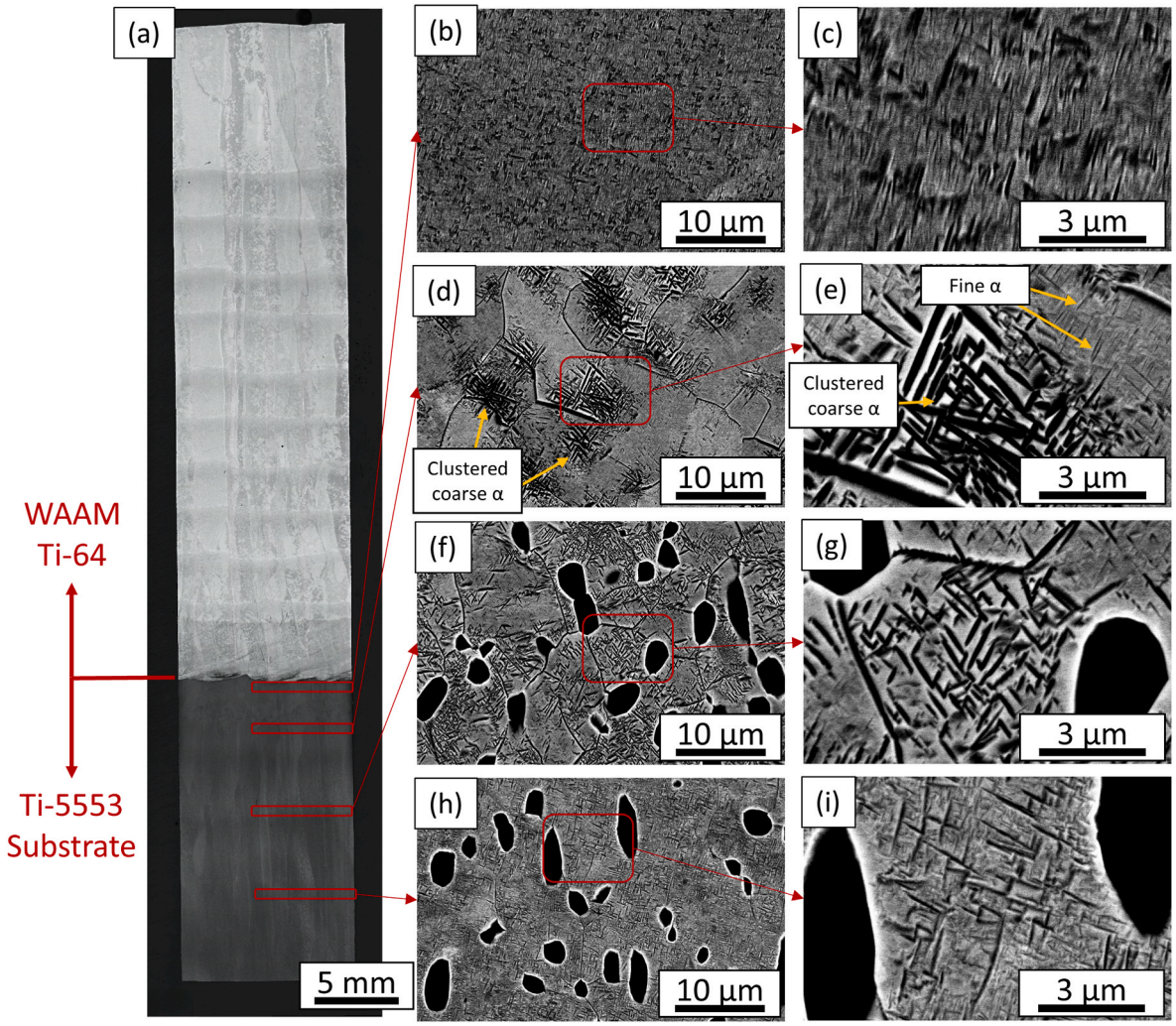

Fig. 8. Microstructural features of the Ti-5553 substrate in the as-deposited condition. Microstructural state of the matrix at different distances from the interfaces are revealed by SEM micrographs recorded at two different magnifications.

nucleation of phases that are too fine to be resolved with SEM or EBSD.

3.3. Microstructural aspects of multi-layer samples

An optical macrograph of a sample extracted across the entire build direction of the as-deposited sample is presented in Fig. 6a. The interface between the Ti-5553 substrate and Ti-64 deposit appears well defined (Fig. 6c). Long columnar β-grains reaching many mm in length are aligned with the build direction, as commonly observed in WAAM fabricated Ti-64 [10,11,16,20–25]. The optical micrograph from the sample after the stress-relief heat-treatment is presented in Fig. 6b. The β-grains appear unaffected from the low temperatures of the heat treatment. The Ti-5553 material adjacent to the interface in the heat-treated sample can be seen to have reacted stronger with the etchant, producing the observed darker contrast observed in the macrograph. Prominent 'HAZ bands' can be observed in the deposited Ti-64 material as annotated in Fig. 6a. These HAZ bands have already been investigated in detail by several other authors during WAAM deposition of Ti-64 [54,55], and therefore not the focus of this work. The observed bands are thought to form upon material that is reheated close to the β-transus temperature. At the base of the band the basketweave α morphology coarsens, experiences greater solute partitioning between the constituent phases, and etches darker; whilst at the top of the band, the microstructure is a finer α lamellar with less solute partitioning and etches brighter [54].

Micrographs captured at various locations through the build height of the deposited Ti-64 material is presented in Fig. 7c–h for both samples. The microstructure consists of a basketweave morphology. Negligible change in microstructure can be observed between the as-deposited and heat-treated samples, which can be attributed to the insensitivity of the Ti-64 alloy to low temperature heat-treatments such as that used in this work. In both the as-deposited and heat-treated samples, finer basketweave α laths can be observed within the initial layer (Fig. 7g and h), and is concurrent with observations of Kennedy et al. who attributed the finer morphology to solute mixing effects between the Ti-64 and Ti-5553 [18].

Fig. 8 presents microstructural features with the Ti-5553 substrate region of the as-deposited sample. At 0.5 mm from the interface a homogenous dispersion of very fine scale α laths can be observed in the SEM micrographs presented in Fig. 8b and c. In the single-track specimen, no α phase was observable within 0.5 mm proximity to the FZ (Fig. 3c). This indicates that the observed α in the multi-layer specimen has precipitated during the cyclic re-heating effect from subsequent layers. The presence of fine sub-β-grains is also not revealed, indicating local β-grain growth must have occurred during exposure to temperature which is above the β-transus. At a distance of 3 mm from the interface, coarse α laths can be observed to form within clusters, separated by regions containing finer α phases (Fig. 8d and e). The existence of fine sub-β-grains in the base metal can still be observed, indicating that this region was exposed to temperatures insufficient to promote β-grain

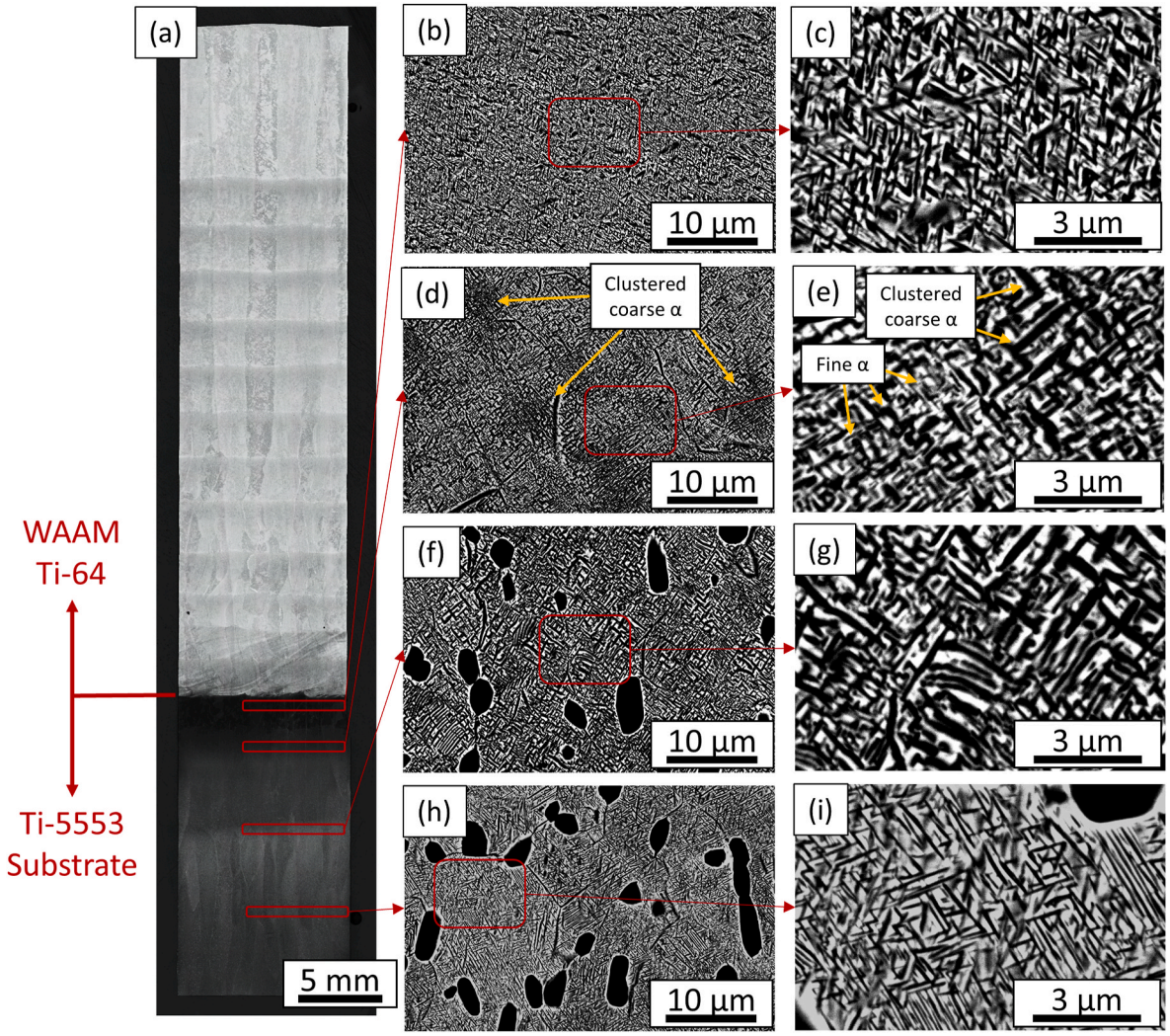

Fig. 9. Microstructural features of the Ti-5553 substrate in the heat-treated sample. Microstructural state of the matrix at different distances from the interfaces are revealed by SEM micrographs recorded at two different magnifications.

growth.

The location and frequency of the clusters of coarse α laths formed are consistent with the globular primary α grains of the base metal (Fig. 2). Analysis of the single-track specimen revealed that during the dissolution of the primary α grains, a region within the Ti-5553 exists where the α grains appear to be dissolved in SEM micrographs (Fig. 3d and e), are no longer indexed as α phase in EBSD results (Fig. 5c), yet still show evidence of chemical segregation with an enrichment of α-stabilisers and depletion of β-stabilisers with EDX (Figs. 4 and 5c). It follows that during subsequent reheating during the deposition of subsequent layers, these diffuse regions of prior globular α grains are favourable locations for α-phase growth than the surrounding matrix. At a distance of 8 mm and beyond from the interface, the globular α grains are visible (Fig. 8f–i). The secondary α laths appear coarser at 8 mm distance from the interface compared to the locations at 13 mm from the interface. The temperature within these regions is insufficient enough for dissolution of the globular α_p grains to occur. However, as already discussed and noted in the single-track sample, the α_s laths tend to dissolve at lower temperature. Therefore, it is possible that partial dissolution and subsequent growth of the α_s laths has occurred during the cyclic thermal fluxes from the deposition of subsequent layers and would explain the difference in α_s morphology between 8 mm and 13 mm from the interface.

The microstructural features of the Ti-5553 substrate of the heat-treated sample are presented in Fig. 9. Compared with the as-deposited sample, the α_s laths appear much more homogenous throughout the build direction. This is particularly noticeable at proximity to the interface, as can be seen in Fig. 9b–e and is consistent with the stronger reaction with the chemical etchant noted in the optical macrograph. Ageing treatments for Ti-5553 are typically used to precipitate α_s to high volume fraction and are usually performed around 450–650 °C such as the stress-relief heat-treatment used within this work. At 3 mm from the interface the α_s laths appear to vary notably in thickness (Fig. 9e). The coarser α_s are again clustered together as in the as-deposited sample (Fig. 8d and e) indicating they have been retained during the heat-treatment and finer α_s laths have precipitated in the surrounding β matrix. At a location of 8 mm from the interface and beyond (Fig. 9f–i) the globular α grains and fine sub-β-grains of the substrate appear unaffected by the heat-treatment. However, the α_s laths appear much more homogenous and well defined.

Based on the observations within this work, a schematic illustration of the microstructure evolution within the Ti-5553 HAZ, based on the proximity to the FZ, is suggested in Fig. 10. Upon deposition of the initial track, the temperature of the substrate adjacent to the FZ is heated sufficiently high to dissolve the α phases and even cause β-grain growth. Subsequent excursion to thermal fluxes during the deposition of subsequent layers or heat treatment allow the α phase to nucleate and grow as fine acicular laths to high volume fraction. At further distance from the Ti-64 interface, there is a region where the partial dissolution of the

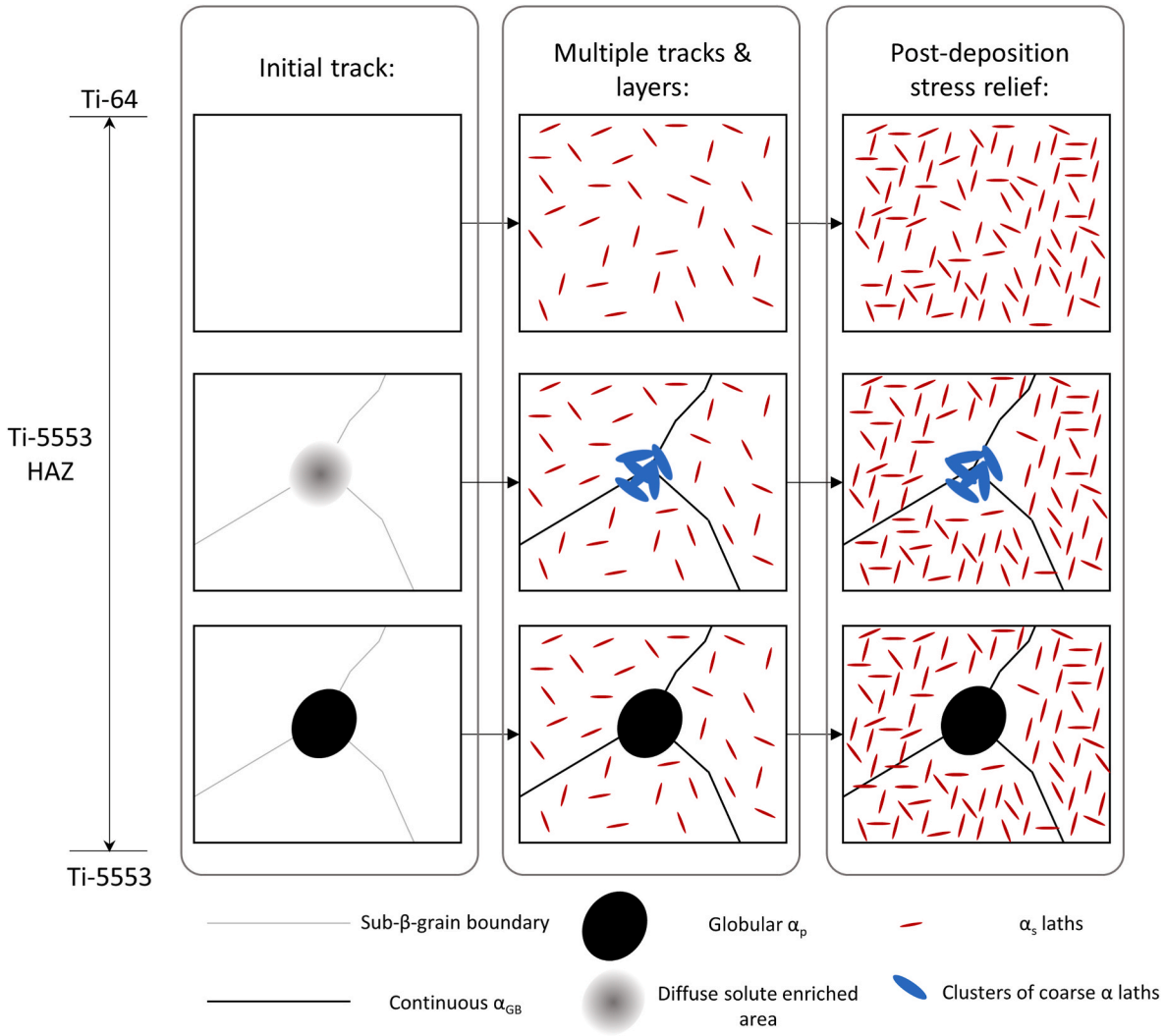

Fig. 10. Schematic illustration of the gradient of microstructural features observed through the HAZ of the Ti-5553 substrate for the case of a single track, multi-layer deposit, as well as following the post-deposition stress relief heat treatment.

globular α_p phase is observed after deposition of the initial track. These regions, enriched with α-stabilising solutes, are preferential locations for subsequent α-phase growth which forms during subsequent exposure to temperature during the deposition of subsequent tracks and layers. Additionally, finer acicular laths will begin to form homogeneously throughout the remaining material producing the observed variation in α lath thickness observed in Fig. 9d. Finally, at further distance from the FZ, the temperature exposure from the initial track is sufficient to dissolve the α_s laths, but insufficient for dissolution of the globular α_p. Subsequent re-heating effects from the deposition of additional tracks and layers allows α-phase to precipitate as fine acicular α laths once again.

3.4. Microhardness of multi-layer samples

Microhardness maps for both the as-deposited and heat-treated samples are presented in Fig. 11. A clear variation in microhardness can be observed between Ti-5553 substrate and the WAAM Ti-64 in both the as-deposited and heat-treated samples. It is also clear that the heat-treatment has had negligible effect on the microhardness, which is consistent with the minor influence the heat-treatment has shown on the microstructure. The microhardness of the Ti-5553 substrate in the as-deposited sample shows a microhardness in the range of 350–440 HV. Following the heat-treatment, the substrate reveals a more uniform microhardness range of 380–425 HV. In both the as-deposited as well as heat-treated samples the WAAM Ti-64 shows a microhardness range of 310–380 HV.

3.5. Residual stress analysis of multi-layer samples

Although it is established that the Ti-64 alloy responds well to stress relief heat treatments at 600 °C, information on stress relaxation behaviour of Ti-5553 is currently lacking. Therefore, residual stress measurements using the contour method were adopted on both the as-deposited as well as heat treated samples to confirm whether the temperature (600 °C) opted for stress-relief heat-treatments is sufficient for relaxation of residual stresses developed in the Ti-5553 alloy substrate. Fig. 12 presents the out-of-plane residual stress measurements across the cross-sectioned surface of the multi-layer samples. A band of tensile residual stress across the base of the substrate of up to 300 MPa can be seen in the as-deposited condition. Development of tensile residual stressed in the substrate is akin to that reported by Szost et al., who used neutron diffraction to measure residual stresses in WAAM deposited Ti-64. Such stresses are thought to develop due to the contraction of newly deposited material upon cooling. In extreme cases this can lead to distortion of the substrate and a pronounced 'bowing' effect that is a frequent issue for weldments and AM parts.

After heat treatment at 600 °C, the stress distribution through the

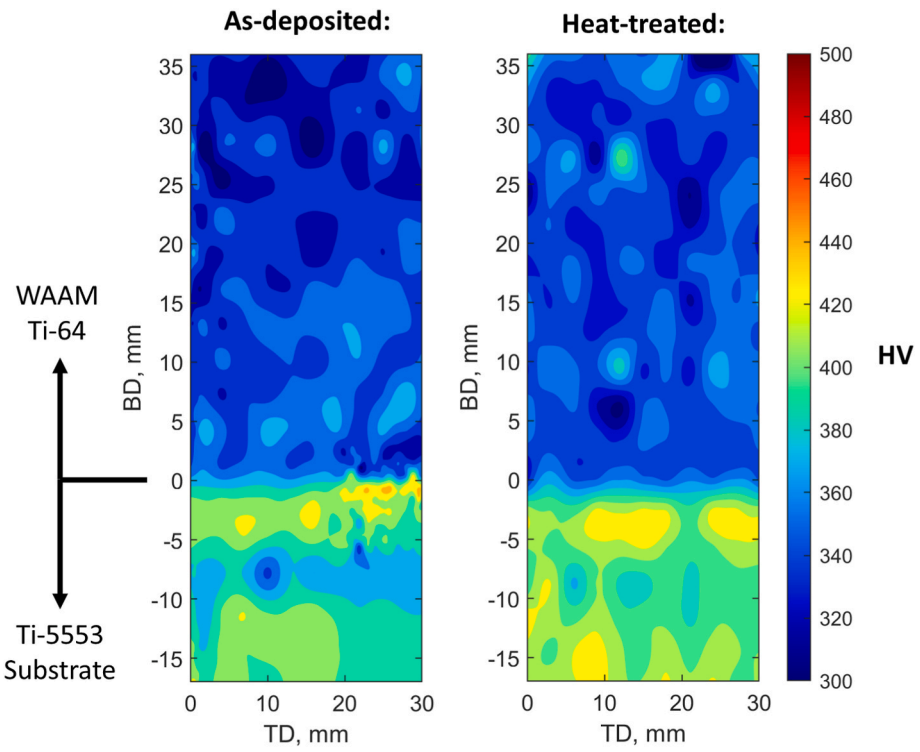

Fig. 11. Microhardness maps of the as-deposited and heat-treated samples.

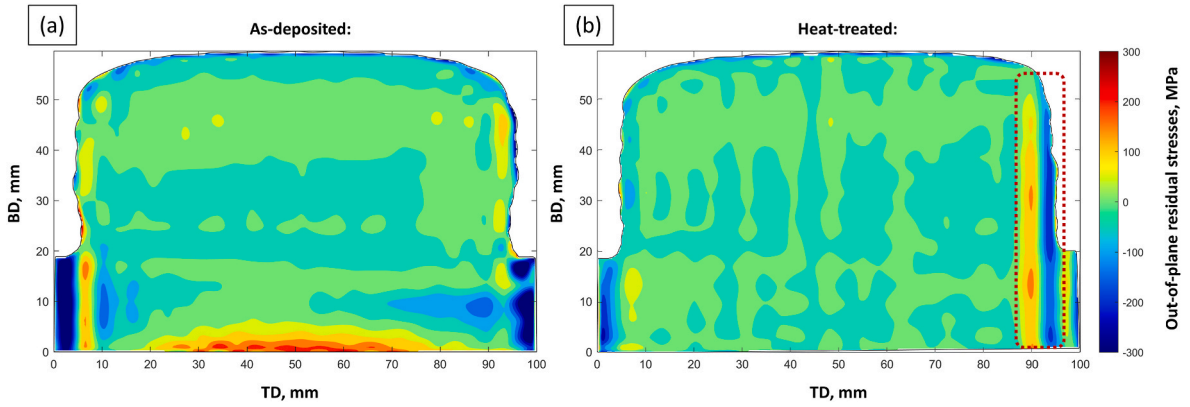

Fig. 12. Out-of-plane residual stress measurements calculated from the contour method across the cross-sectioned surfaces of the as-deposited (a) and heat-treated (b) samples. Note the red annotated rectangle on (b) to indicate the location of a wire-breakage artefact.

Table 2
Tensile properties of as-deposited as well as heat-treated samples.

Condition	Location and orientation	YS, MPa	UTS, MPa	El, %
As-deposited	Interface BD	872.3 ± 10.9	930.3 ± 11.0	6.2 ± 2.8
	Deposit BD	815.3 ± 5.2	884.3 ± 6.4	15.3 ± 2.3
Heat-treated	Interface BD	887.5 ± 14.1	924.7 ± 17.8	9.8 ± 2.1
	Deposit BD	846.6 ± 7.6	895.7 ± 6.5	15.4 ± 2.3
	Deposit TD	887.3 ± 7.6	940.7 ± 4.0	7.7 ± 2.0

build direction appears uniform with complete relaxation noted at the base of the substrate. Note that due to wire-breakage during w-EDM a cutting induced artefact can be observed in the residual stress plot, as annotated in Fig. 12b. These results indicate that 600 °C for 8 h appears adequate for reliving the residual stresses from the AAC.

3.6. Tensile properties of multi-layer samples

The tensile properties of samples extracted from the different locations are presented in Table 2, and representative flow curves from each condition are presented in Fig. 13. In general, all samples tested can be observed to begin yielding at stresses >815 MPa and show minor strain hardening effects with an average of 53 MPa increase noted between YS and UTS. In the as-deposited and heat-treated samples tested across the WAAM Ti-64 and Ti-5553 interface failure occurred across the gauge region of the Ti-64. This can be attributed to the exceptional strength of the Ti-5553 alloy and is an indication of high strength within the Ti-5553 HAZ even in the as-deposited condition. Samples extracted from the WAAM Ti-64 demonstrate greater ability to deform during deformation than those extracted across the interface for both as-deposited

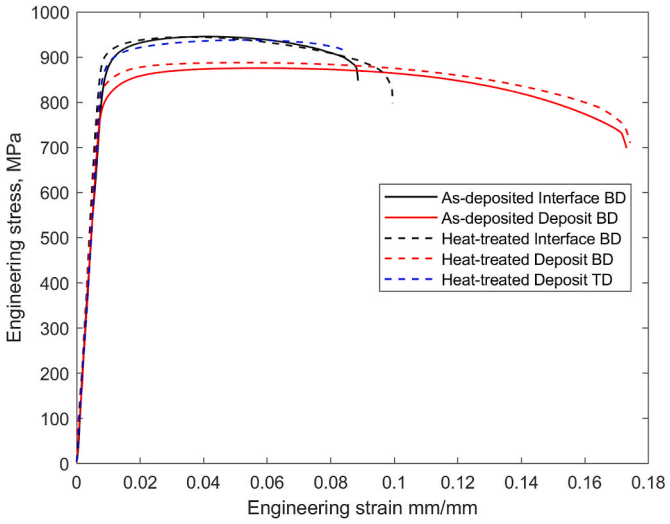

Fig. 13. Representative flow curves of samples tested from blocks of as-deposited and heat-treated conditions.

condition as well as after heat-treatment. This can be attributed to the generally poorer ductility of the Ti-5553 alloy which shares a portion of the gauge length for these samples, therefore reducing the total ability for the tensile coupon to elongate prior to failure.

Notable anisotropy can be observed in the deposited Ti-64 material by comparing the heat-treated Deposit BD and Deposit TD specimens. The TD oriented coupons show greater strength, but poorer ductility, and is consistent with reports from other authors who attribute such behaviour to the anisotropic β grain structure [10,22–24]. The heat-treatment appears to have had an overall minor improvement on the yield strength of the Interface BD and Deposit BD coupons, and in particular an improvement to the elongation at fracture of the Interface BD coupons. These results suggest that this heat-treatment appears promising to simultaneously stress relieve such AAC structures, whilst retaining the globular α grains and fine sub-β-grain microstructure of the bulk Ti-5553 forging.

4. Conclusions

In this work, Ti-64 alloy was deposited using WAAM on Ti-5553 forged substrates that had been solution treated and aged as typically required for high-strength aerospace structural applications. Some samples were exposed to a stress-relief heat-treatment. Analysis of the deposited material and substrate was conducted to understand the microstructure, residual stresses, microhardness and tensile properties.

- Analysis of a single-track of Ti-64 deposited on Ti-5553 revealed a gradient microstructure through the HAZ. At the periphery of the HAZ, α_s laths were found to dissolve first, followed by the globular α_p grains with closer proximity to the FZ. Incomplete dissolution of the globular α_p grains was noted due to the rapid thermal flux from the melt-pool which was insufficient to allow homogenisation of the alloying elements. This was observed as diffuse regions of β-phase still enriched with α-stabilizers and depleted in β-stabilizers that could act as preferential regions for subsequent α nucleation and growth.
- In the multi-layer samples, the as-deposited Ti-64 material was characterised with a fine basketweave α morphology and long columnar β-grains aligned with the build direction. The HAZ of the Ti-5553 revealed inhomogeneous α-lath morphologies through the HAZ which was attributed to the complex dissolution, precipitation, and growth of α phase during the cyclic thermal fluxes during deposition of multiple layers.
- Tensile testing in the as-deposited condition was characterised with a UTS of 884 MPa and ductility of 15 % for samples aligned with the build direction. Samples tested across the interface all failed in the WAAM Ti-64 material and demonstrated greater strength but poorer ductility.
- Residual stress analysis using the contour method indicated that a band of tensile residual stresses observed in the substrate was relaxed after the heat-treatment at 600 °C. This is complemented by the formation of a more homogeneous α phase noted throughout the Ti-5553 HAZ, as well as retention of the globular α_p grains and fine sub-β-grain morphology in the base metal.
- The heat-treatment showed minor improvements to the yield strength and ductility of the tested conditions. Notable anisotropy was noted in the WAAM Ti-64 material, with greater strength and poorer ductility for samples loaded perpendicular to the build direction.

Overall, this work demonstrates the feasibility for features of the Ti-64 alloy to be deposited using WAAM on forged Ti-5553 substrates.

Data availability

Data will be made available on request.

CRediT authorship contribution statement

Calum Hicks: Investigation, Formal analysis, Writing – original draft, Visualization. **Saeed Tamimi:** Investigation, Writing – review & editing. **Giribaskar Sivaswamy:** Investigation, Writing – review & editing. **Misael Pimentel:** Project administration, Writing – review & editing. **Scott McKegney:** Investigation, Writing – review & editing. **Stephen Fitzpatrick:** Project administration.

Declaration of competing interest

The authors declare that they have no known competing financial interests or personal relationships that could have appeared to influence the work reported in this paper.

Acknowledgement

The authors sincerely acknowledge the funding supports from Aerospace Technology Institute (ATI) under the *AFRC_DIFG_-CRAD_1941_Hybrid Direct Energy Deposition* project, and thanks to Safran Landing Systems Services UK Ltd for donating the initial billet used for this Collaborative Research and Development (CR&D) project.

References

[1] Kolli RP, et al. A review of metastable beta titanium alloys, vol. 8; 2018. p. 1–41.
[2] Jackson M, et al. Titanium and its alloys: processing, fabrication and mechanical performance. 2010.
[3] Hatefi A. Direct laser fabrication of Ti-5553. 2013.
[4] Jiankai M, et al. Microstructure and mechanical properties of forging-additive hybrid manufactured Ti–6Al–4V alloys. Mater Sci Eng 2021;811:140984.
[5] Chakraborty D, et al. The state of the Art for wire Arc Additive manufacturing process of titanium alloys for aerospace applications. J Mater Eng Perform 2022;31 (8):6149–82.
[6] Sword JI, Galloway A, Toumpis A. An environmental impact comparison between wire + arc additive manufacture and forging for the production of a titanium component. Sustainable Materials and Technologies 2023;36(e00600).
[7] Hasani N, et al. Dislocations mobility in superalloy-steel hybrid components produced using wire arc additive manufacturing. Mater Des 2022:220.
[8] Shekhar S, et al. Effect of solution treatment and aging on microstructure and tensile properties of high strength β titanium alloy, Ti–5Al–5V–5Mo–3Cr 2015;66: 596–610.
[9] Panza-Gios R. The effect of heat treatment on the microstructure evolution and mechanical properties of Ti-5Al-5V-5Mo-3Cr, and its potential application in landing gears. 2009.
[10] Wang F, et al. Microstructure and mechanical properties of wire and arc additive manufactured Ti-6Al-4V 2013;44:968–77.

[11] Vázquez L, et al. Influence of interpass cooling conditions on microstructure and tensile properties of Ti-6Al-4V parts manufactured by WAAM, vol. 64; 2020. p. 1377–88.
[12] Stolf P. Machinability Comparison between two different Grades of titanium alloys under Diverse Turning and cooling conditions: Ti-6Al-4V and Ti-5Al-5V- 5Mo-3Cr. 2019.
[13] DebRoy T, et al. Additive manufacturing of metallic components – Process, structure and properties 2018;92:112–224.
[14] Ding J, et al. Production of large metallic components by additive manufacture - Issues and Achievements. 2015.
[15] Williams SW, et al. Wire + Arc Additive manufacturing, vol. 32; 2016. p. 641–7.
[16] Bermingham MJ, et al. Optimising the mechanical properties of Ti-6Al-4V components produced by wire + arc additive manufacturing with post-process heat treatments 2018;753:247–55.
[17] Bai X, et al. Numerical analysis of heat transfer and fluid flow in multilayer deposition of PAW-based wire and arc additive manufacturing 2018;124:504–16.
[18] Kennedy JR, et al. Microstructure transition gradients in titanium dissimilar alloy (Ti-5Al-5V-5Mo-3Cr/Ti-6Al-4V) tailored wire-arc additively manufactured components 2021;182:111577.
[19] Davis AE, et al. Mechanical performance and microstructural characterisation of titanium alloy-alloy composites built by wire-arc additive manufacture 2019;765: 138289.
[20] Szost BA, et al. A comparative study of additive manufacturing techniques: residual stress and microstructural analysis of CLAD and WAAM printed Ti-6Al-4V components, vol. 89; 2016. p. 559–67.
[21] Wang J, et al. Effects of subtransus heat treatments on microstructure features and mechanical properties of wire and arc additive manufactured Ti–6Al–4V alloy 2020;776:139020.
[22] Baufeld B, Van Der Biest O. Mechanical properties of Ti-6Al-4V specimens produced by shaped metal deposition, vol. 10; 2009.
[23] Baufeld B, et al. Wire based additive layer manufacturing: Comparison of microstructure and mechanical properties of Ti-6Al-4V components fabricated by laser-beam deposition and shaped metal deposition, vol. 211; 2011. p. 1146–58.
[24] Bambach M, et al. Hybrid manufacturing of components from Ti-6Al-4V by metal forming and wire-arc additive manufacturing 2020;282:116689.
[25] Antonysamy A. Microstructure, texture and mechanical property evolution during additive manufacturing of Ti6Al4V alloy for aerospace applications. 2012.
[26] Zhang J, et al. Effect of Interlayer-Compressed argon gas active cooling on microstructure and properties of Ti–6Al–4V fabricated by WAAM. Adv Eng Mater 2023;25(20):2300618.
[27] Zhu YY, et al. Solidification behavior and grain morphology of laser additive manufacturing titanium alloys, vol. 777; 2019. p. 712–6.
[28] Lutjering G, Williams JC. Titanium. second ed. 2007. p. 1–442.
[29] Fanning JC. Properties of TIMETAL 555 (Ti-5Al-5Mo-5V-3Cr-0.6Fe). 2005.
[30] Jones NG, et al. Thermomechanical processing of Ti-5Al-5Mo-5V-3Cr, vol. 490; 2008. p. 369–77.
[31] Hicks C, et al. Anisotropic tensile properties and failure mechanism of laser metal deposited Ti–5Al–5Mo–5V–3Cr alloy before and after sub-transus heat-treatment, vol. 825; 2021, 141928.
[32] Sen M, et al. Tensile deformation mechanism and failure mode of different microstructures in Ti–5Al–5Mo–5V–3Cr alloy 2019;753:156–67.
[33] Schwab H, et al. Processing of Ti-5553 with improved mechanical properties via an in-situ heat treatment combining selective laser melting and substrate plate heating, vol. 130; 2017.
[34] Schwab H, et al. Microstructure and mechanical properties of the near-beta titanium alloy Ti-5553 processed by selective laser melting, vol. 105; 2016.
[35] Gao J. Understanding the relationship between microstructure and mechanical properties in HIPped Ti-5Al-5Mo-5V-3Cr. 2018.
[36] Nag S, et al. Omega-Assisted nucleation and growth of Alpha precipitates in the Ti-5Al-5Mo-5V-3Cr-0.5Fe Beta titanium alloy 2009;57:2136–47.
[37] Nag S, et al. Non-classical homogeneous precipitation mediated by compositional fluctuations in titanium alloys, vol. 60; 2012. p. 6247–56.
[38] Jiang B, et al. Microstructural evolution and its effect on the mechanical behavior of Ti-5Al-5Mo-5V-3Cr alloy during aging, vol. 731; 2018. p. 239–48.
[39] Kar SK, et al. Quantitative microstructural characterization of a near beta Ti alloy, Ti-5553 under different processing conditions 2013;81:37–48.
[40] Nag S, et al. Elemental partitioning between α and β phases in the Ti–5Al–5Mo–5V–3Cr–0.5Fe (Ti-5553) alloy 2009;89:535–52.
[41] Foltz JW, et al. Formation of grain boundary α in β Ti alloys: its role in deformation and fracture behavior of these alloys, vol. 42; 2011. p. 645–50.
[42] Liu CM, et al. Subtransus triplex heat treatment of laser melting deposited Ti-5Al-5Mo-5V-1Cr-1Fe near β titanium alloy, vol. 590; 2014. p. 30–6.
[43] Liu C, et al. Influence of continuous grain boundary α on ductility of laser melting deposited titanium alloys, vol. 661; 2016. p. 145–51.
[44] Qin D, et al. Tensile deformation and fracture of Ti-5Al-5V-5Mo-3Cr-1.5Zr-0.5Fe alloy at room temperature 2013;587:100–9.
[45] Prime MB, DeWald AT. The contour method. 2013. p. 109–38.
[46] Hosseinzadeh F, et al. Towards good practice guidelines for the contour method of residual stress measurement. J Eng 2014;2014:453–68.
[47] Chen F, et al. Isochronal phase transformation in bimodal Ti-55531, vol. 9; 2019.
[48] Chen F, et al. Isothermal kinetics of β ↔ α transformation in Ti-55531 alloy influenced by phase composition and microstructure, vol. 130; 2017. p. 302–16.
[49] Pereloma E, et al. Microstructure development and alloying elements diffusion during sintering of near-β titanium alloys, vol. 520; 2012. p. 49–56.
[50] Semiatin SL, et al. Dissolution of the Alpha phase in Ti-6Al-4V during Isothermal and continuous heat treatment, vol. 50; 2019. p. 2356–70.
[51] Ballat-Durand D, et al. Multi-scale and multi-technic microstructure analysis of a linear friction weld of the metastable-β titanium alloy Ti-5Al-2Sn-2Zr-4Mo-4Cr (Ti17) towards a new Post-Weld Heat Treatment 2018;144:661–70.
[52] Song J, et al. Crack initiation and short crack propagation of friction stir welded TC17 alloy joint. Int J Fatig 2023:168.
[53] Campo KN, et al. Exploring the Ti-5553 phase transformations utilizing in-situ high-temperature laser-scanning confocal microscopy. Mater Char 2020;159.
[54] Ho A, et al. On the origin of microstructural banding in Ti-6Al4V wire-arc based high deposition rate additive manufacturing 2019;166:306–23.
[55] Kelly SM, Kampe SL. Microstructural evolution in Laser-Deposited multilayer Ti6Al-4V build: Part I. Microstructural characterization. Metall Mater Trans 2004; 35:1861–7.